

Observation of Feshbach resonances between a single ion and ultracold atoms

<https://doi.org/10.1038/s41586-021-04112-y>

Received: 19 May 2021

Accepted: 8 October 2021

Published online: 15 December 2021

 Check for updates

Pascal Weckesser¹✉, Fabian Thielemann¹, Dariusz Wiater², Agata Wojciechowska², Leon Karpa^{1,3}, Krzysztof Jachymski², Michał Tomza², Thomas Walker^{1,4} & Tobias Schaeetz^{1,4}

The control of physical systems and their dynamics on the level of individual quanta underpins both fundamental science and quantum technologies. Trapped atomic and molecular systems, neutral¹ and charged², are at the forefront of quantum science. Their extraordinary level of control is evidenced by numerous applications in quantum information processing^{3,4} and quantum metrology^{5,6}. Studies of the long-range interactions between these systems when combined in a hybrid atom–ion trap^{7,8} have led to landmark results^{9–19}. However, reaching the ultracold regime—where quantum mechanics dominates the interaction, for example, giving access to controllable scattering resonances^{20,21}—has so far been elusive. Here we demonstrate Feshbach resonances between ions and atoms, using magnetically tunable interactions between ¹³⁸Ba⁺ ions and ⁶Li atoms. We tune the experimental parameters to probe different interaction processes—first, enhancing three-body reactions^{22,23} and the related losses to identify the resonances and then making two-body interactions dominant to investigate the ion’s sympathetic cooling¹⁹ in the ultracold atomic bath. Our results provide deeper insights into atom–ion interactions, giving access to complex many-body systems^{24–27} and applications in experimental quantum simulation^{28–30}.

At ultracold temperatures, the collisions between particles reveal their quantum mechanical nature. Considering a classical collision between two spheres, a decrease in temperature results in reduced velocities and lower reaction rates. However, in the quantum regime, where wave–particle duality becomes dominant, a lower temperature results in an expansion of the particles’ de Broglie wavelength. In a simplified way, the related increase in overlap leads to a possible enhancement in the collision rates. In fact, Wigner threshold laws predict a finite reaction rate even at zero temperature. For small but finite energies, the quantization of angular momentum l leads to the emergence of centrifugal barriers, which prevent the scattering into channels of higher partial waves. This allows for a simplified view based on a small number of parameters. Here, the particles’ wavefunction is well defined by its energy and a global phase. In the case of elastic collisions of atoms or molecules, the kinetic energy in the centre-of-mass frame remains conserved. Thus, only the phase of the scattered wave function can be altered. It experiences a phase shift, which can be related to the scattering length a . This single parameter determines cross-sections and, for given densities, collision rates. Furthermore, a can be tuned and resonantly enhanced, if the free state of the colliding particles matches the energy and couples to a quasibound molecular state. If the magnetic moments of the free and quasibound states are different, magnetic fields can be exploited to tune these into resonance using the differential Zeeman shift. This phenomenon is known as magnetic Feshbach resonance.

During the past two decades, Feshbach resonances have become a powerful and versatile tool to control the short-range contact interaction in homonuclear and heteronuclear alkali atomic mixtures^{31,32}, alkali–closed-shell atomic combinations³³ and atom–molecule systems³⁴. The application of Feshbach resonances to longer-range interparticle interactions has so far been limited to few highly magnetic lanthanide atoms^{35,36}. It has been proposed that the combination of atoms and ions would be a suitable candidate to introduce an isotropic, $1/r^4$ interaction potential to the quantum toolbox. Here r is the interatomic distance. Its large characteristic range of thousands of Bohr radii⁸, is predicted to enable novel applications in quantum simulation³⁰ and quantum information processing^{28,29}. Hybrid atom–ion systems have been widely studied and typically combine radiofrequency (RF) traps for the ion with optical dipole traps for the atoms. However, Feshbach resonances have not been observed in such systems for two reasons. On the one hand, the s -wave scattering regime for atom–ion systems is energetically at least two orders of magnitude lower than for the neutral counterpart⁸. On the other hand, the ion trap’s oscillating RF fields heat the ion during elastic collisions, resulting in kinetic energies of the ion exceeding the atomic temperature by several orders of magnitude^{14,37–40}. The combination of both effects prevents the atom–ion mixture from reaching the few-partial-wave regime—a critical prerequisite for the observation of Feshbach resonances. However, it has been conjectured³⁷ that few atom–ion combinations, such as ¹³⁸Ba⁺–⁶Li or ¹⁷¹Yb⁺–⁶Li, would be suitable to reach the few-partial-wave regime in

¹Albert-Ludwigs-Universität Freiburg, Physikalisches Institut, Freiburg, Germany. ²Faculty of Physics, University of Warsaw, Warsaw, Poland. ³Leibniz University Hannover, Institute of Quantum Optics, Hannover, Germany. ⁴EUCOR Centre for Quantum Science and Quantum Computing, Albert-Ludwigs-Universität Freiburg, Freiburg, Germany. ✉e-mail: pascal.weckesser@physik.uni-freiburg.de

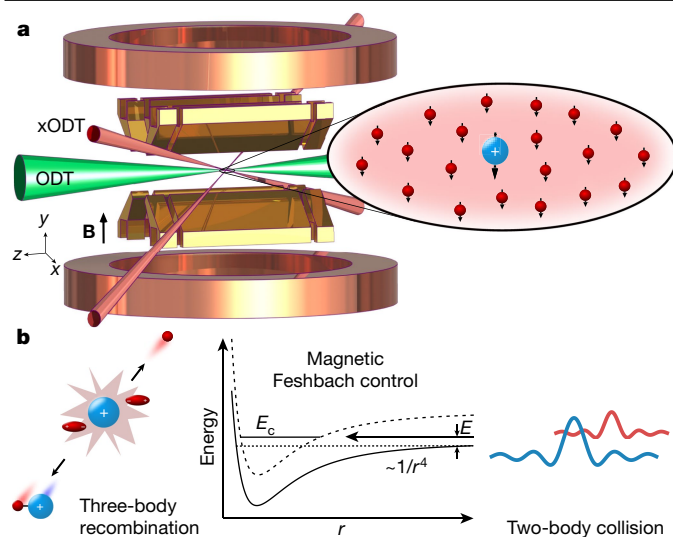


Fig. 1 | Experimental setup and concepts. **a**, We store a single $^{138}\text{Ba}^+$ ion in a linear segmented RF trap, optionally in an ODT in absence of any RF fields. Simultaneously, we prepare an ultracold ^6Li ensemble in an xODT. Polarizing the spins of the fermionic Li atoms suppresses mutual atom–atom interactions via the Pauli exclusion principle. By using a set of Helmholtz coils, we apply a homogeneous magnetic field B . **b**, We control the atom–ion interactions by magnetic Feshbach resonances. Here, two particles colliding in an open channel at energy E couple to a closed-channel molecular bound state E_c of relative magnetic moment $\delta\mu$. Tuning B or choosing various n and t_{int} allows the observation of different processes, such as elastic two-body collisions (illustrated by quantum mechanical wave packets) and inelastic TBR (classical hard spheres). Although the former permits sympathetic cooling of the ion into the few-partial-wave regime where the particles behave as waves, the latter can lead to the formation of weakly bound molecular ions followed by loss.

a hybrid trap, as the RF-induced heating is substantially reduced for systems of large ion-to-atom mass ratio. Recently, collision energies that allow access to the single-partial-wave regime have been demonstrated for $\text{Yb}^+ - \text{Li}$ (ref. ¹⁹).

Here we demonstrate the observation of Feshbach resonances between a single $^{138}\text{Ba}^+$ ion and ^6Li atoms. We find a total of eleven resonances and identify four of them as s -wave resonances. Varying the atomic density n , we find three-body recombination to be the predominant loss channel for ions in the vicinity of a Feshbach resonance. Reducing n allows us to tune the atom–ion sympathetic cooling rate. To confirm this, we exploit optical trapping of the ion^{41–43}—paving the way for a common optical confinement of atom–ion ensembles in the absence of detrimental RF fields⁴⁴.

Experimental protocol

We load and confine single $^{138}\text{Ba}^+$ ions deterministically in the RF trap⁴³ (trap frequency $\Omega_{\text{rf}} = 2\pi \times 1.433$ MHz and secular frequencies $\omega_{x,y,z}^{\text{Ba}^+} = 2\pi \times \{123, 122, 7.6\}$ kHz). We cool the ions close to the Doppler limit $T_D \approx 365$ μK , compensate stray electric fields down to 3 mV m^{-1} and prepare them in an incoherent spin mixture of $|6S_{1/2}; s^{\text{Ba}^+} = 1/2, m_s^{\text{Ba}^+} = \pm 1/2\rangle$ through optical pumping, where s and m_s are the electronic spin angular momentum and its projection onto the quantization axis (for the electronic-level scheme, see Extended Data Fig. 1). We then displace the Ba^+ ion from the trap centre by applying dc control fields. Next, we create and store a cloud of $11 \times 10^3 - 33 \times 10^3$ ^6Li atoms with a temperature $T_{\text{Li}} = 1 - 3$ μK and a density $n = 5 \times 10^{11} - 33 \times 10^{11}$ in a crossed optical dipole trap (xODT) at the RF trap centre (Methods, Fig. 1a). We then apply a tunable magnetic field B of up to 320 G and return the ion to the trap centre where it is located inside the atomic cloud. We choose Li in the hyperfine state $|2\rangle = |f^{\text{Li}} = 1/2, m_f^{\text{Li}} = -1/2\rangle$,

where f and m_f are the total angular momentum and the respective projection onto the quantization axis, allowing for efficient polarization of Ba^+ into the $|s^{\text{Ba}^+} = 1/2, m_s^{\text{Ba}^+} = -1/2\rangle$ magnetic sublevel during the first few collisions, similar to refs. ^{13,17,18}. For the ground state $|1\rangle = |f^{\text{Li}} = 1/2, m_f^{\text{Li}} = +1/2\rangle$, spin relaxation is forbidden to first order. The ion and atoms are allowed to interact for a variable interaction duration $t_{\text{int}} \in [100, 300]$ ms. Finally, we use fluorescence detection to derive the survival probability P_{ion} of the Ba^+ in the RF trap (Methods). Instead of detecting the ion’s state in the RF trap, we may transfer it to a single-beam optical dipole trap (ODT) for 500 μs , in complete absence of Li and RF fields. As the ODT is chosen to be relatively shallow, it enforces an energy cut-off for ions exceeding a dedicated kinetic energy limit. As a result, we obtain a finite optical trapping probability p_{opt} (ref. ⁴⁵), allowing us to benchmark the sympathetic cooling efficiency via the atoms. Finally, we may optionally detect the Li atom number and temperature with absorption imaging around $B_{\text{Li}} \approx 293$ G.

Locating atom–ion Feshbach resonances

As we operate with a large number of atoms ($N_{\text{atom}} > 10^4$) and a single ion, atom loss through atom–ion interactions is negligible. Therefore, to perform loss spectroscopy, we search for Feshbach resonances by probing the Ba^+ loss, which we detect with near-unity efficiency. Unlike in loss spectroscopy with atomic quantum gases, where the particles are irretrievably lost from the trap, the comparatively deep RF trap can store some ionic reaction products. The details of how these reaction products are distinguished can be found in Methods.

For guidance, ab initio electronic structure calculations and multichannel quantum scattering calculations (MCQSC) are used to predict the number of resonances, their mutual distances and their approximate width Δ_0^{theor} . However, the prediction of their absolute magnetic field location B_0^{theor} requires input from experimental observation. For our system, we expect relevant contributions of partial waves for $l \leq 2$ (s, p and d). MCQSC forecasts about 5(1) Feshbach resonances, including s, p - and d -wave resonances, for $B \in [70, 330]$ G with $\Delta_0^{\text{theor}} \approx 1$ G. For this calculation, we considered regular, that is, spin-projection-conserving electronic interaction only ($\delta m_F = 0$ with $m_F = m_f^{\text{Li}} + m_s^{\text{Ba}^+}$).

To reveal these resonances experimentally, we performed a point-by-point search of B_0^{expt} with a step size of about 400 mG (Fig. 2). For each located resonance, we adapt t_{int} to obtain $P_{\text{ion}} \lesssim 50\%$ on resonance. Despite investigating only parts of the range $B \in [70, 330]$ G, we already observe 11 resonances (Extended Data Table 1). It is noted that ^6Li prepared in spin state $|2\rangle$ with no Ba^+ present does not feature any resonances within the investigated B -field ranges.

Theoretical resonance assignment

The observed number of resonances (11) exceeds the initial prediction by MCQSC (about 5(1)). This indicates that additional coupling terms besides regular electronic interaction have to be considered, such as the second-order spin–orbit coupling (SOC). As SOC can substantially mix the internal spins (m_f) with the rotational motion (l, m_l), the number of resonances would be increased⁴⁶. Note that m_f -changing couplings can also split and shift higher partial-wave resonances^{46,47}, whereas s -wave resonances remain unaffected to first order. Here we use the term l -wave resonances if the entrance collision channel is coupled to an l -wave molecular level.

As an initial step towards a complete partial-wave assignment, we first attempt to identify the s -wave resonances with $|\delta m_F| = \{0, 1, 2\}$, the positions of which depend only on the singlet and triplet scattering lengths a_s and a_T . The first nine discovered resonances were used to obtain best-fit values for a_s and a_T from the asymptotic bound-state model (Methods). From this, three s -wave resonances (all $\delta m_F = 1$) were identified and an additional one with $\delta m_F = 1$ was predicted around $B_{0,s}^{\text{theor}} = 172$ G. Subsequently, we observed a resonance at $B_0^{\text{expt}} = 173.0(2)$ G, which is strong

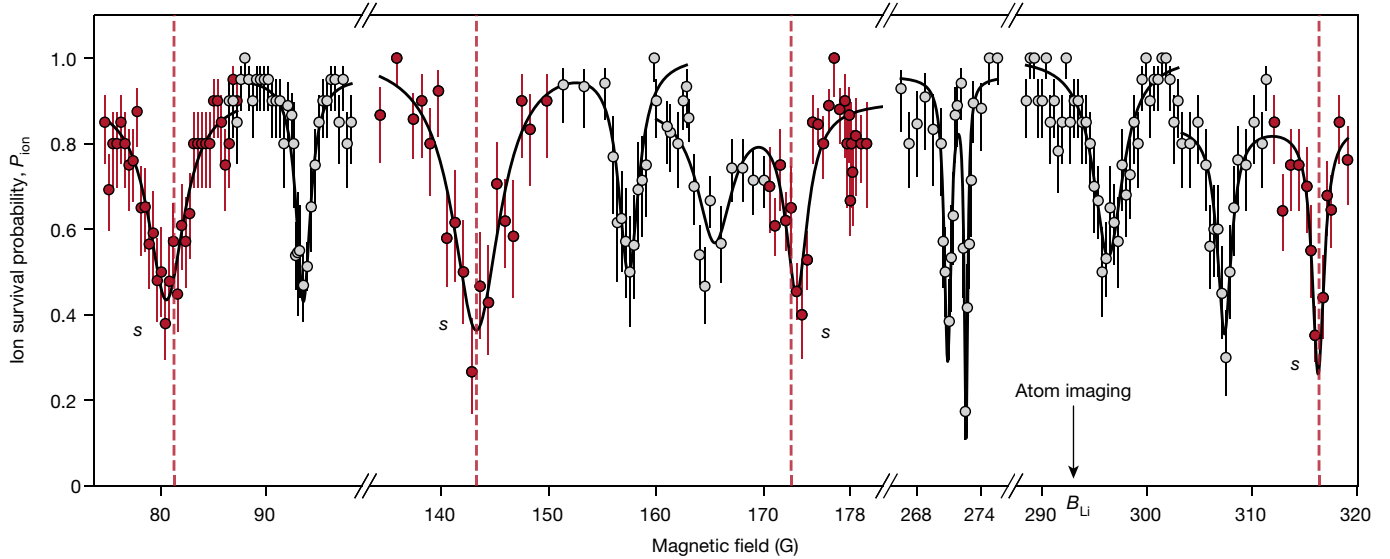


Fig. 2 | Detection of atom–ion Feshbach resonances by magnetic-field-dependent ion loss spectroscopy. The dependence of P_{ion} for a single $^{138}\text{Ba}^+$ ion embedded into $20(2) \times 10^3$ spin-polarized ^6Li atoms on B and given t_{int} . The experimental data (circles) represent an average of at least 20 experimental realizations and the error bars denote the 1σ confidence interval. The data were taken in random order for a given resonance. We obtain

evidence for correct s -wave assignment. We find $a_s = 0.236R_4$ and $a_T = -0.053R_4$ ($R_4 = 69$ nm) using all four s -wave resonances (Methods). Note that one can derive the scattering length a from a_s and a_T . The presented accuracy of the assignment is comparable to those typically achieved for Feshbach resonances of neutral atoms. To provide an assignment for $l \geq 1$, a refined model is currently under investigation.

Atomic-density-dependent ion loss

Independent of the current assignment, we further examine the nature of the Ba^+ loss processes and their dynamics. To study the number of atoms involved in the loss process of the ion and the related timescales, we probe the dependence of P_{ion} on t_{int} for five different n . We selected the Feshbach resonance at 296.31 G, as it lies closest to B_{Li} . Here we derive n with the highest accuracy, while we avoid larger changes of the B field, potentially sweeping over atom–ion resonances not yet identified. For each time evolution, we fit an exponential decay $e^{-t_{\text{int}}\Gamma_{\text{Loss}}}$, with Γ_{Loss} being the $1/e$ ion loss rate (Extended Data Fig. 2).

The results for $\Gamma_{\text{Loss}}(n)$ are illustrated in Fig. 3. We model the data by $\Gamma_{\text{Loss}}(n) = k_2n + k_3n^2$, with k_2 and k_3 representing the two-body and three-body loss rate coefficients. We derive $k_3 = 7.8_{-2.5}^{+3.9} \times 10^{-25} \text{ cm}^6 \text{ s}^{-1}$ whereas k_2 remains consistent with zero. Alternatively, we fit the exponent c of $\Gamma_{\text{Loss}}(n) \propto n^c$, resulting in $c = 2.02(29)$. We conclude that the ion losses are dominated by three-body recombination (TBR)^{22,23}. The increase of TBR in the vicinity of a Feshbach resonance is directly related to the enhancement of two-body interaction. Note that TBR occurs despite operating with a spin-polarized fermionic atomic ensemble obeying the Pauli exclusion principle. In a simplified picture, the Fermi wavelength and the related Pauli repulsion are significantly reduced as the atom slides down the $1/r^4$ potential and gains substantially in kinetic energy.

The process of TBR and the related width of a resonance is strongly temperature dependent⁴⁸. Resolving Feshbach resonances down to a full-width at half-maximum (FWHM) of 0.4(1) G, we can estimate an upper bound for the collision energy E_{col} in the two-body centre-of-mass frame. Here we assume that Δ_0^{expt} solely results from temperature broadening and we take the maximal differential magnetic moment for a two-valence-electron system ($\delta\mu = 4\mu_B$, where μ_B is the Bohr magneton).

the centre position of the resonances B_0^{expt} and their FWHM Δ_0^{expt} (Extended Data Table 1) by fitting a sum of Lorentzian functions to the data points (black curve). We assign four s -wave resonances (red data points). Their theoretical positions $B_{0,s}^{\text{theor}}$ are represented by the red vertically dashed lines. It is noted that we can independently characterize the atomic cloud by high-field absorption imaging around $B_{\text{Li}} \approx 293$ G.

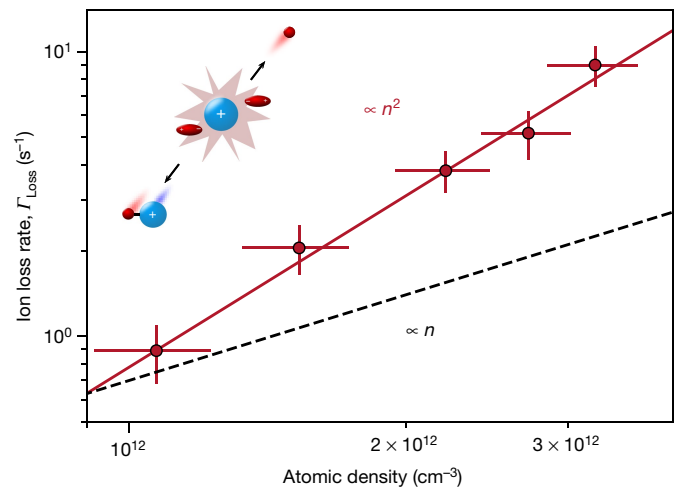


Fig. 3 | Dependence of the ion loss rate on the atomic density at the Feshbach resonance at 296.31 G. The vertical errors represent the 1σ confidence interval of the fit. The horizontal errors represent the systematic uncertainty of the atomic density, due to fluctuations in atom–ion overlap and atom number. The red solid line shows the best fit for $\Gamma_{\text{Loss}}(n) = k_2n + k_3n^2 \approx k_3n^2$ obtained by bootstrapping. To emphasize the deviation of a linear dependency on n , which is the expected scaling for two-body loss channels, we also present a linear scaling (dashed black line).

This coarse estimate based on the Breit–Wigner formula indicates that such narrow resonances only become detectable for $E_{\text{col}} \lesssim 50 \mu\text{K} \times k_B$ (where k_B is the Boltzmann constant), regardless of their partial wave character. Note that E_{col} amounts to the height of the centrifugal barrier of d -wave scattering ($E_d = 77.4 \times k_B$) and is on the same order as our experimental conservative upper bound ($\lesssim 90 \mu\text{K} \times k_B$; Methods).

Magnetic tunability of cross-sections

To study the predicted versatility of atom–ion Feshbach resonances, we investigate the prospects of controlling our experimental parameters

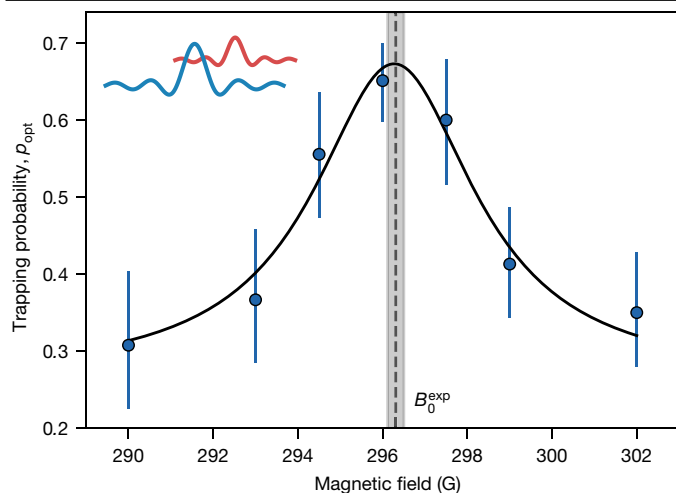


Fig. 4 | Enhanced sympathetic cooling in the vicinity of the Feshbach resonance at 296.31 G. After interacting for $t_{\text{int}} = 150$ ms with the Li atoms, we transfer the Ba^+ ion into the shallow ODT with fixed trap depth $U_0^{\text{ODT}} = 620(113) \mu\text{K} \times k_B$ and record the p_{opt} dependence on B . The data points are an average of up to 86 independent realizations and were recorded in random order. The error bars denote the 1σ confidence interval. In the vicinity of the Feshbach resonance at $B_0^{\text{exp}} = 296.31(19)$ G (vertical dashed line with respective error bars denoted as the shaded area), we observe a maximum for p_{opt} , which is strong evidence for enhanced sympathetic cooling owing to an increase of the elastic cross-section σ_2 . Fitting the data with a phenomenological Lorentzian function (black solid curve) results in a centre position of $296.3(2)$ G and a FWHM of $4.6(1.1)$ G, which is consistent with B_0^{exp} .

to mitigate TBR losses while enhancing the sympathetic cooling of the Ba^+ ion by elastic two-body collisions with the Li atoms. For a direct comparison of two-body and three-body collisions, we again operate close to $B_0^{\text{exp}} = 296.31$ G. We decrease n and t_{int} to $5.5(2.0) \times 10^{11} \text{cm}^{-3}$ and 150 ms, respectively, resulting in an ion survival probability P_{ion} of $95.7_{-6.5}^{+2.7}\%$ for identical RF confinement in the hybrid trap. Under these conditions, we probe the dependence of the sympathetic cooling efficiency on B . Following the interaction with the atoms, we transfer the Ba^+ ion into the ODT of trap depth $U_0^{\text{ODT}} = 620(113) \mu\text{K} \times k_B$. It is noted that after the interaction, the actual energy distribution of the ion deviates from an ideal Boltzmann distribution, for example, as the ion has not reached its kinetic steady state for the chosen t_{int} and as RF-heating effects typically result in non-thermal Tsallis distributions⁴⁰. As a consequence, we cannot derive a temperature representing the ion's kinetic energy E_{Ba^+} as presented in ref.⁴⁵. Nevertheless, the optical trapping probability p_{opt} is directly related to E_{Ba^+} , that is, for lower E_{Ba^+} we expect higher p_{opt} and vice versa.

Running the experimental protocol in absence of atom–ion interaction, we observe $p_{\text{opt}} < 5\%$. Operating with atom–ion interaction detuned by $|B - B_0^{\text{exp}}| > \Delta_0^{\text{exp}}$ from resonance, we record $p_{\text{opt}} \approx 30\%$ (Fig. 4). Tuning to B_0^{exp} , we observe a further increase towards $p_{\text{opt}} \approx 65\%$. We see this as evidence for enhanced sympathetic cooling related to an increase of the elastic two-body cross-section $\sigma_2(\mathbf{B})$, a key attribute of Feshbach resonances.

Conclusions and future perspectives

We have observed magnetically tunable Feshbach resonances between a single ion and an ultracold atomic gas. Depending on the atomic density, we found the tunable atom–ion interactions to be dominated by either two-body or three-body collisions.

Moving beyond this demonstration, we will extend the control over the interactions of choice by coherently controlling the electronic degrees of freedom of $^{138}\text{Ba}^+$ including deterministic state-preparation and investigating ^6Li in its hyperfine ground state. Further optimizing

the sympathetic cooling might enable an all-optical approach⁴⁴, where the ion(s) and atoms are confined in an optical trap simultaneously, in the absence of disturbing RF fields and their detrimental heating mechanisms. This is predicted to permit studying chemistry in the s-wave regime, where molecular ions can be formed coherently by magneto or RF association⁴⁹, as well as stored and analysed after exothermic reactions, for example, via deep box-shaped RF potentials⁵⁰. Further experimental data on certain resonances will allow for improvements to the accuracy and detail of predictions from MCQSC. This might provide deeper insight into the molecular structure at short range, where additional interactions, such as SOC, shift and split resonances⁴⁶. Furthermore, exploiting Feshbach resonances in a generic atom–ion ensemble might find application in many-body systems, such as polaron^{25,26} and impurity physics²⁷ as well as experimental quantum simulations^{28–30}.

Online content

Any methods, additional references, Nature Research reporting summaries, source data, extended data, supplementary information, acknowledgements, peer review information; details of author contributions and competing interests; and statements of data and code availability are available at <https://doi.org/10.1038/s41586-021-04112-y>.

- Bloch, I., Dalibard, J. & Zwirger, W. Many-body physics with ultracold gases. *Rev. Mod. Phys.* **80**, 885–964 (2008).
- Leibfried, D., Blatt, R., Monroe, C. & Wineland, D. Quantum dynamics of single trapped ions. *Rev. Mod. Phys.* **75**, 281–324 (2003).
- Wineland, D. Nobel lecture: Superposition, entanglement, and raising Schrödinger's cat. *Rev. Mod. Phys.* **85**, 1103–1114 (2013).
- Saffman, M., Walker, T. & Mølmer, K. Quantum information with Rydberg atoms. *Rev. Mod. Phys.* **82**, 2313–2363 (2010).
- Katori, H. Optical lattice clocks and quantum metrology. *Nat. Photon.* **5**, 203–210 (2011).
- Micke, P. et al. Coherent laser spectroscopy of highly charged ions using quantum logic. *Nature* **578**, 60–65 (2020).
- Härter, A. & Hecker Denschlag, J. Cold atom–ion experiments in hybrid traps. *Contemp. Phys.* **55**, 33–45 (2014).
- Tomza, M. et al. Cold hybrid ion–atom systems. *Rev. Mod. Phys.* **91**, 035001 (2019).
- Grier, A., Cetina, M., Oručević, F. & Vuletić, V. Observation of cold collisions between trapped ions and trapped atoms. *Phys. Rev. Lett.* **102**, 223201 (2009).
- Rellergert, W. G. et al. Measurement of a large chemical reaction rate between ultracold closed-shell ^{40}Ca atoms and open-shell $^{174}\text{Yb}^+$ ions held in a hybrid atom–ion trap. *Phys. Rev. Lett.* **107**, 243201 (2011).
- Ratschbacher, L., Zipkes, C., Sias, C. & Köhl, M. Controlling chemical reactions of a single particle. *Nat. Phys.* **8**, 649–652 (2012).
- Hall, F., Aymar, M., Raoult, M., Dulieu, O. & Willitsch, S. Light-assisted cold chemical reactions of barium ions with rubidium atoms. *Mol. Phys.* **111**, 1683–1690 (2013).
- Ratschbacher, L. et al. Decoherence of a single-ion qubit immersed in a spin-polarized atomic bath. *Phys. Rev. Lett.* **110**, 160402 (2013).
- Meir, Z. et al. Dynamics of a ground-state cooled ion colliding with ultracold atoms. *Phys. Rev. Lett.* **117**, 243401 (2016).
- Saito, R. et al. Characterization of charge-exchange collisions between ultracold ^6Li atoms and $^{40}\text{Ca}^+$ ions. *Phys. Rev. A* **95**, 032709 (2017).
- Joger, J. et al. Observation of collisions between cold Li atoms and Yb^+ ions. *Phys. Rev. A* **96**, 030703 (2017).
- Fürst, H. et al. Dynamics of a single ion–spin impurity in a spin-polarized atomic bath. *Phys. Rev. A* **98**, 012713 (2018).
- Sikorsky, T., Meir, Z., Ben-Shlomi, R., Akerman, N. & Ozeri, R. Spin-controlled atom–ion chemistry. *Nat. Commun.* **9**, 920 (2018).
- Feldker, T. et al. Buffer gas cooling of a trapped ion to the quantum regime. *Nat. Phys.* **16**, 413–416 (2020).
- Idziaszek, Z., Simoni, A., Calarco, T. & Julienne, P. Multichannel quantum-defect theory for ultracold atom–ion collisions. *New J. Phys.* **13**, 083005 (2011).
- Tomza, M., Koch, C. & Moszynski, R. Cold interactions between an Yb^+ ion and a Li atom: prospects for sympathetic cooling, radiative association, and Feshbach resonances. *Phys. Rev. A* **91**, 042706 (2015).
- Härter, A. et al. Single ion as a three-body reaction center in an ultracold atomic gas. *Phys. Rev. Lett.* **109**, 123201 (2012).
- Krükow, A., Mohammadi, A., Härter, A. & Denschlag, J. H. Reactive two-body and three-body collisions of Ba^+ in an ultracold Rb gas. *Phys. Rev. A* **94**, 030701 (2016).
- Cote, R., Kharchenko, V. & Lukin, M. Mesoscopic molecular ions in Bose–Einstein condensates. *Phys. Rev. Lett.* **89**, 093001 (2002).
- Casteels, W., Tempere, J. & Devreese, J. Polaronic properties of an ion in a Bose–Einstein condensate in the strong-coupling limit. *J. Low Temp. Phys.* **162**, 266–273 (2011).
- Jachymski, K. & Negretti, A. Quantum simulation of extended polaron models using compound atom–ion systems. *Phys. Rev. Res.* **2**, 033326 (2020).
- Hirzler, H. et al. Controlling the nature of a charged impurity in a bath of Feshbach dimers. *Phys. Rev. Res.* **2**, 033323 (2020).
- Doerk, H., Idziaszek, Z. & Calarco, T. Atom–ion quantum gate. *Phys. Rev. A* **81**, 012708 (2010).

29. Gerritsma, R. et al. Bosonic Josephson junction controlled by a single trapped ion. *Phys. Rev. Lett.* **109**, 080402 (2012).
30. Bissbort, U. et al. Emulating solid-state physics with a hybrid system of ultracold ions and atoms. *Phys. Rev. Lett.* **111**, 080501 (2013).
31. Inouye, S. et al. Observation of Feshbach resonances in a Bose–Einstein condensate. *Nature* **392**, 151–154 (1998).
32. Inouye, S. et al. Observation of heteronuclear Feshbach resonances in a mixture of bosons and fermions. *Phys. Rev. Lett.* **93**, 183201 (2004).
33. Barbé, V. et al. Observation of Feshbach resonances between alkali and closed-shell atoms. *Nat. Phys.* **14**, 881–884 (2018).
34. Yang, H. et al. Observation of magnetically tunable Feshbach resonances in ultracold $^{23}\text{Na}^{40}\text{K} + ^{40}\text{K}$ collisions. *Science* **363**, 261–264 (2019).
35. Aikawa, K. et al. Bose–Einstein condensation of erbium. *Phys. Rev. Lett.* **108**, 210401 (2012).
36. Durastante, G. et al. Feshbach resonances in an erbium–dysprosium dipolar mixture. *Phys. Rev. A* **102**, 033330 (2020).
37. Cetina, M., Grier, A. & Vuletić, V. Micromotion-induced limit to atom–ion sympathetic cooling in Paul traps. *Phys. Rev. Lett.* **109**, 253201 (2012).
38. Chen, K., Sullivan, S. T. & Hudson, E. R. Neutral gas sympathetic cooling of an ion in a Paul trap. *Phys. Rev. Lett.* **112**, 143009 (2014).
39. Höltkemeier, B., Weckesser, P., López-Carrera, H. & Weidemüller, M. Buffer-gas cooling of a single ion in a multipole radio frequency trap beyond the critical mass ratio. *Phys. Rev. Lett.* **116**, 233003 (2016).
40. Rouse, I. & Willitsch, S. Superstatistical energy distributions of an ion in an ultracold buffer gas. *Phys. Rev. Lett.* **118**, 143401 (2017).
41. Lambrecht, A. et al. Long lifetimes and effective isolation of ions in optical and electrostatic traps. *Nat. Photon.* **11**, 704–707 (2017).
42. Schmidt, J. et al. Optical trapping of ion Coulomb crystals. *Phys. Rev. X* **8**, 021028 (2018).
43. Weckesser, P. et al. Trapping, shaping, and isolating of an ion Coulomb crystal via state-selective optical potentials. *Phys. Rev. A* **103**, 013112 (2021).
44. Schmidt, J., Weckesser, P., Thielemann, F., Schaetz, T. & Karpa, L. Optical traps for sympathetic cooling of ions with ultracold neutral atoms. *Phys. Rev. Lett.* **124**, 053402 (2020).
45. Schneider, C., Enderlein, M., Huber, T., Dürr, S. & Schaetz, T. Influence of static electric fields on an optical ion trap. *Phys. Rev. A* **85**, 013422 (2012).
46. Ticknor, C., Regal, C., Jin, D. & Bohn, J. Multiplet structure of Feshbach resonances in nonzero partial waves. *Phys. Rev. A* **69**, 042712 (2004).
47. Cui, Y. et al. Observation of broad *d*-wave Feshbach resonances with a triplet structure. *Phys. Rev. Lett.* **119**, 203402 (2017).
48. Maier, T. et al. Emergence of chaotic scattering in ultracold Er and Dy. *Phys. Rev. X* **5**, 041029 (2015).
49. Köhler, T., Góral, K. & Julienne, P. Production of cold molecules via magnetically tunable Feshbach resonances. *Rev. Mod. Phys.* **78**, 1311 (2006).
50. Wester, R. Radiofrequency multipole traps: tools for spectroscopy and dynamics of cold molecular ions. *J. Phys. B* **42**, 154001 (2009).

Publisher's note Springer Nature remains neutral with regard to jurisdictional claims in published maps and institutional affiliations.

© The Author(s), under exclusive licence to Springer Nature Limited 2021

Preparation of spin-polarized ${}^6\text{Li}$ ensemble

To prepare our ${}^6\text{Li}$ ensemble, we first load a magneto-optical trap and then transfer the atoms into an xODT. During the transfer into the xODT, we optically pump the Li atoms into the lowest two hyperfine states $|1\rangle = |f^{\text{Li}} = 1/2, m_f^{\text{Li}} = +1/2\rangle$ and $|2\rangle = |f^{\text{Li}} = 1/2, m_f^{\text{Li}} = -1/2\rangle$, producing an incoherent 50/50 mixture. We then switch to higher magnetic fields $B \approx 345.9$ G to increase the elastic cross-section between the ${}^6\text{Li}$ atoms⁵¹. Gradually lowering the power of the xODT over 900 ms as in ref.⁵², we evaporatively cool the atomic cloud and obtain approximately 40×10^3 ${}^6\text{Li}$ atoms with final temperatures on the order of 1–3 μK . For the lowest temperatures, we obtain typical trapping frequencies $\omega_{x,y,z}^{\text{Li}} = 2\pi \times \{1.77(10), 1.94(10), 0.19(1)\}$ kHz. Finally, we prepare the Li ensemble in spin state $|2\rangle$ through spin-selective absorption imaging of state $|1\rangle$ for 100 μs at $B \approx 345.9$ G. We detect the Li atoms in spins state $|2\rangle$ by applying high-field absorption imaging at $B \approx 293$ G. We can further determine the temperature of the atomic ensemble T_{Li} by time-of-flight thermometry⁵³.

The crossed dipole trap

The xODT is created by a commercial solid-state laser at 1,064 nm with a maximum output power of 50 W. The trap consists of two linearly polarized laser beams with orthogonal polarization crossing at an angle of about 14° . Here both k vectors intersect the \hat{x} – \hat{z} plane and the ion trap's principal axis \hat{z} at an angle of about 7° and about 31° , respectively. The foci of the two beams are overlapped and the beam waists are 30(3) μm . We superimpose the centre of the xODT with the ion by maximizing the a.c. Stark shift caused by the xODT on the ion. We validate the atom–ion overlap with an independent reference measurement. Similar to ref.¹⁶, we probe the atomic density profile by recording the ion loss rate for a Ba^+ ion being prepared in the $5D_{3/2}$ manifold. We find consistency between the two methods.

Optical trapping of ${}^{138}\text{Ba}^+$ ions in the ODT

After the atom–ion interaction, we can transfer the Ba^+ ion into the single-beam ODT. The ODT is operated at 532 nm and propagates along the \hat{z} axis of the RF trap (\hat{z}). The beam waists equal $w_x = 4.5(2)$ μm and $w_y = 4.0(2)$ μm at the location of the ion. It is noted that the ODT acts attractively for Ba^+ prepared in the $6S_{1/2}$ manifold⁴³, whereas it is blue-detuned, and thus repulsive, for the Li atoms. Independent calibration measurements show that the presence of the atoms does not influence the ion's optical trapping probability p_{opt} , as the repulsive ODT separates the ensemble from the ion on timescales of less than 100 μs . Transferring the ion into the ODT and turning off the RF fields follows the experimental protocol as in ref.⁴³. At the end, we transfer the ion back into the linear RF trap and detect it via fluorescence imaging while Doppler cooling. If we detect an ion in the RF trap, we consider the optical trapping attempt successful. If we observe no ion, the ion was irretrievably lost from the ODT and the attempt was unsuccessful. Repeating the protocol, we obtain the optical trapping probability p_{opt} . It is noted that we do not record a significant change in p_{opt} by applying an external magnetic field up to 300 G.

Calculating the electro-optical trap depth

Unlike for neutral atoms where the potential trap depth predominantly depends on the a.c. Stark shift⁵⁴, the Ba^+ ion is subject to the Coulomb interaction and therefore very sensitive to electric fields⁵⁵. The electro-optical potential is therefore given by three contributions: (1) the a.c. Stark shift, (2) residual stray electric fields and (3) d.c. defocusing curvatures. During an optical trapping attempt, we confine the ion along the ODT's k vector ($k \parallel \hat{z}$) using d.c. contributions. It is noted that an axial d.c. confinement inevitably results in defocusing in the radial \hat{x} – \hat{y} plane⁵⁶. Independent calibration measurements reveal radial stray electric fields and radial defocusing d.c. curvatures of $E_s \leq 3$ mV m⁻¹ and $m_{\text{Ba}^+}\omega_{\text{dc}}^2$ with

m_{Ba^+} being the ion mass and $\omega_{\text{dc}}^2 = -(2\pi \times 6.5(1))^2 \text{kHz}^2$, respectively. Knowing the beam waist and the electrical contributions, we derive the electro-optical trap depth U_0^{ODT} as presented in ref.⁴³.

Probing the ion survival probability

During the atom–ion interaction, the Ba^+ ion might undergo various processes in the hybrid trap. The ion can collide elastically, meaning it remains in the $6S_{1/2}$ electronic ground state while exchanging energy with the Li atoms, acting as cooling agent. In contrast, the ion might undergo an inelastic spin-changing collision or TBR^{22,23,57,58}. The latter predominantly results in the formation of weakly bound molecular ions^{58,59} followed by loss. The losses can be partially explained by a combination of collisional quenching and light-assisted dissociation. For the latter, the ion can gain significant kinetic energy, change its electronic state or undergo a non-radiative charge exchange resulting in neutral Ba and in charged Li^+ . Except for the case of charge exchange, the Ba^+ ion remains within the deep trapping volume of the Paul trap and its presence can be detected by fluorescence imaging. Similar observations have recently been reported for Ba^+ –Rb (ref.⁶⁰). However, the exact mechanism remains to be investigated for Ba^+ –Li.

To reliably discriminate between elastic and inelastic collisions, we apply the following protocol. In a first step, we apply Doppler cooling using laser light at 493 nm and 650 nm (see energy levels and related transitions in Extended Data Fig. 1). Here, we operate the 493-nm cooling laser close to resonance, with a detuning of $\delta = -2/3\Gamma$ with $\Gamma = 2\pi \times 15.2$ MHz being the natural linewidth of the excited $6P_{1/2}$ state. For this detuning, we can detect cold Ba^+ ions populating the $6S_{1/2}$ manifold. If detected, we consider this a survival event where the ion interacted purely elastically with the Li atoms. To detect Ba^+ of increased kinetic energy E_{kin} , for example, owing to photodissociation ($> 100 \text{K} \times k_B$), we apply an additional far red-detuned cooling laser with $\delta \approx -14\Gamma$ for 1 s. This laser is able to cool the ions of increased E_{kin} into the subkelvin regime, where they become detectable by the nearer-detuned fluorescence imaging beam. Taking a second fluorescence image, we detect those ions. As final measurement, we examine whether the ion populates the metastable $5D_{5/2}$ manifold. Here, we apply laser light at 614 nm, optically pumping the ion into the electronic ground state via the $6P_{3/2}$ state (Extended Data Fig. 1). Taking a third fluorescence image, we can detect these ions. In the case that we do not detect any ion, we assume the Ba^+ to have undergone charge exchange. For the ion loss spectroscopy in Fig. 2, P_{ion} is defined by the number of survival events divided by the total number of events (elastic and inelastic). Inelastic events are the sum of ions of increased E_{kin} , ions populating the $5D_{5/2}$ manifold and non-detectable ions. Note that the emergence of ions populating the $5D_{5/2}$ amounts to about 50% of all losses. We found that this ratio is dependent on the amplitude of the magnetic field we apply.

To probe for the potential formation of weakly bound molecular ions by TBR, we optionally apply an extended protocol. Here we apply an additional ion loading cycle to provide an ion Coulomb crystal for sympathetic cooling of the molecular ion via the directly laser-cooled crystal and allowing for its indirect detection, as well as vibrational mass spectrometry. After loading, we included waiting durations of up to several minutes; however, we were never successful in the observation of a molecular ion.

Estimating a lower and upper bound for the collision energy

The atom–ion interaction is carried out in presence of oscillating RF fields. The collision energy is therefore given by the energy of the respective particles (E_{Li} and E_{Ba^+}) and the contributions of intrinsic and excess micromotion (E_{IMM} and E_{EMM})¹⁹:

$$E_{\text{coll}} = \frac{\mu}{m_{\text{Li}}} E_{\text{Li}} + \frac{\mu}{m_{\text{Ba}^+}} (E_{\text{Ba}^+} + E_{\text{IMM}} + E_{\text{EMM}}). \quad (1)$$

Here μ , m_{Ba^+} and m_{Li} are the reduced mass, the ion mass and the atom mass, respectively. Applying time-of-flight thermometry, we obtain $E_{\text{Li}} = 3/2k_{\text{B}}/T_{\text{Li}}$ with $T_{\text{Li}} = 1.3(2) \mu\text{K}$. We estimate the ion's average kinetic energy E_{Ba^+} in a series of independent measurements. There we investigate the sympathetic cooling dynamics of a single ion embedded in the cloud of ultracold atoms by repeatedly transferring the ion into the ODT while probing p_{opt} for variable U_0^{ODT} (ref. 45). For half the density, as used in Fig. 2, we observe the ion to reach a kinetic steady state (about $100 \mu\text{K} \times k_{\text{B}}$) within the first 100 ms. As a consequence, the majority of the observed resonances were measured at the steady-state already.

We can use these independent reference measurements to derive a lower and upper bound of the collision energy. For the lower bound, we make use of the energy scale of about $100 \mu\text{K} \times k_{\text{B}}$. Assuming that the excess micromotion contributions are alike, we estimate a lower bound on the order of more than $17 \mu\text{K} \times k_{\text{B}}$. It is noted that this energy would already allow the presence of p -wave resonances. For a conservative upper bound, we use the energy of a single Doppler-cooled ion that has not undergone sympathetic cooling ($E_{\text{Ba}^+} \lesssim 3/2 \times 600 \mu\text{K} \times k_{\text{B}}$). Again assuming $E_{\text{iMM}} \approx E_{\text{eMM}} \lesssim 600 \mu\text{K} \times k_{\text{B}}$, we derive collision energies of $E_{\text{col}} \lesssim 90 \mu\text{K} \times k_{\text{B}}$. It is noted that this value is on the same order as the theoretical estimate $\lesssim 50 \mu\text{K} \times k_{\text{B}}$ and the centrifugal barrier of d -wave scattering ($E_{\text{d}} = 77.4 \mu\text{K} \times k_{\text{B}}$). Furthermore, the presented energy scales strongly indicate that the observed ions of increased kinetic energy of the previous subsection cannot be explained by micromotion-induced heating.

Magnetic field calibration

Magnetic field calibration is achieved by driving a resonant magnetic-field dependent nuclear spin transition in ${}^6\text{Li}$ between the states $|1\rangle \leftrightarrow |2\rangle$. We determine and benchmark the magnetic fields using the Breit–Rabi formula⁶¹. The calibration was carried out in the vicinity of all recorded Feshbach resonances from Extended Data Table 1. Here we sampled the entire magnetic field range of [80, 320] G with equidistant data points and interpolated intermittent values by a global linear fit function. We derive a systematic magnetic field uncertainty of 60 mG, including day-to-day drifts and minor deviations due to the interpolation. As an independent validation, we probed the $|1\rangle$ – $|1\rangle$ and $|2\rangle$ – $|2\rangle$ atomic p -wave Feshbach resonance in ${}^6\text{Li}$ around 159 G and 215 G, respectively, finding agreement with previous publications⁶².

List of scanned magnetic field ranges

During our investigation, we scanned the following magnetic field ranges: [5,100] G, [118,190] G, [265,280] G and [285,320] G. Figure 2 illustrates the magnetic field windows of the ranges within which we identified Feshbach resonances. For the remaining parts, we did not record any resonance with significant signal-to-noise ratio. Here we typically scanned magnetic subsets of up to 10 G on one day.

Electronic structure calculations

Potential energy curves for the singlet $\chi^1\Sigma^+$ and triplet $a^3\Sigma^+$ molecular electronic states, resulting from the interaction between a ground-state Ba^+ ion and a Li atom, are calculated using ab initio electronic structure approaches, such as the coupled cluster method restricted to single, double and non-iterative triple excitations and the multireference configuration interaction method restricted to single and double excitations with aug-cc-pwCV5Z basis sets and ECP46MDF small-core pseudopotential for Ba^+ to include scalar relativistic effects. A computational scheme following ref. 21 is employed.

The crossing between the $a^3\Sigma^+$ and $b^3\Pi$ molecular electronic states below the collision atomic threshold is predicted (Extended Data Fig. 3). It provides a mechanism for large spin–orbit mixing and large second-order spin–orbit interaction responsible for strong spin-non-conserving scattering^{63,64}.

Multichannel quantum scattering calculations

Two-body collisions are studied using numerically exact multichannel quantum scattering calculations in free space⁸. The Hamiltonian used for the nuclear motion includes the singlet and triplet molecular electronic states, the molecular rotation, the hyperfine and Zeeman interactions, and the interatomic spin–spin interaction resulting from the magnetic dipolar and second-order SOCs. The total scattering wave function is constructed in a complete basis set containing electronic spins, nuclear spins and rotational angular momenta. Experimental values of atomic parameters are assumed. The scattering lengths of the calculated singlet (S) and triplet (T) potentials are adjusted by applying uniform scaling factors λ_i (with $i = \{S, T\}$) to the interaction potentials: $V_i(r) \rightarrow \lambda_i V_i(r)$. The scattering lengths are expressed in units of the characteristic length scale for the atom–ion interaction $R_4 = \sqrt{\mu C_4/\hbar}$, where C_4 and \hbar are the potential coefficient and the reduced Planck constant, respectively. The coupled-channel equations are solved using QDYN²¹ based on S -matrix formalism. Our theoretical approach neglects the impact of the micromotion, trap confinement and Lorentz force on atom–ion scattering. Therefore, the assigned singlet and triplet scattering lengths should be considered as effective ones including shifts by neglected effects.

Asymptotic-bound-state model

The spectrum of bound molecular levels and positions of Feshbach resonances are obtained using the asymptotic-bound-state model (ABM)^{65,66}. The same Hamiltonian and wave-function representation as in the multichannel quantum scattering calculations are employed. The ABM model is used for straightforward and fast assignment of resonance positions and nature of underlying molecular levels.

Assignment of resonances

The positions of Feshbach resonances, B_i^{theo} , are calculated for a set of 10^4 combinations of the singlet, a_s , and triplet, a_t , scattering lengths within the ABM model. A grid equidistant in the scattering phase shifts between $-\pi/2$ and $\pi/2$ is used. Resonances between the collision channel $m_f = -1$ and all coupled channels are located.

Next the predicted theoretical positions of Feshbach resonances are compared with measured positions B_i^{expt} . The singlet and triplet scattering lengths corresponding to experimental data are derived by minimizing the χ^2 function

$$\chi^2(a_s, a_t) = \sum_{i=1}^{N_{\text{expt}}} (B_i^{\text{expt}} - B_i^{\text{theo}}(a_s, a_t))^2, \quad (2)$$

which quantifies how well our theoretical model reproduces the measured positions for N_{expt} datapoints. The related root-mean-square deviation r.m.s.d. = $\sqrt{\chi^2/N_{\text{expt}}}$ can also be used to measure the agreement between theory and experiment.

For the initial assignment, we used resonances resulting from coupling to s -wave molecular levels because such resonances are not affected by the SOC in the first order of perturbation theory. Initially, nine loss features at 80.47 G, 93.59 G, 143.29 G, 157.42 G, 270.86 G, 272.59 G, 296.31 G, 307.41 G, 316.31 G were measured, which were more numerous than number of possible s -wave resonances in studied magnetic field range. Therefore, we calculated χ^2 for all possible subsets of measured features and all combinations of scattering lengths. Two-element subsets could be reproduced by several combinations of scattering lengths and, thus, were insufficient to derive an unambiguous assignment, whereas four and more element subsets could not be described by the used theoretical model. Among a few possible three-element sets, only one would require the existence of an additional s -wave resonance around 172 G, which next was measured around the predicted position. Finally, we found the best agreement for four loss features at the 80.47 G, 143.29 G, 173.0 G and 316.31 G

Article

reproduced as *s*-wave resonances by the ABM model with $\chi^2 = 0.78 \text{ G}^2$ and r.m.s.d. = 0.44 G. The found optimal scattering lengths were $a_s = 0.236R_4$ and $a_{\uparrow} = -0.053R_4$. The second relatively small χ^2 for four *s*-wave resonances was 3.5 times larger than the optimal one. Other possible assignments for a larger number of *s*-wave resonances would result in a significantly larger χ^2 .

The existence of higher partial-wave resonances was neglected in this assignment but similar agreement for higher-wave resonances was obtained with the optimal set of the scattering lengths, whereas other assignments were not able to reproduce all the measured features. A detailed study of higher partial-wave resonances will be presented in the future.

Data availability

The experimental and theoretical data that support the findings of this study are available from the corresponding author upon request. Source data are provided with this paper.

Code availability

The experimental data were analysed using JupyterLab and a self-written analysis script. Electronic structure calculations were performed with the MOLPRO package of *ab initio* programs⁶⁷ and multichannel quantum scattering calculations were realized with the extended version of QDYN program⁶⁸. AMB model results were obtained and analysed with a self-written program and scripts in Mathematica and Python. The simulation results can be generated using the numerical methods described within Methods and the computer code developed, which are available upon request.

51. Jochim, S. et al. Magnetic field control of elastic scattering in a cold gas of fermionic lithium atoms. *Phys. Rev. Lett.* **89**, 273202 (2002).
52. Luo, L. et al. Evaporative cooling of unitary Fermi gas mixtures in optical traps. *New J. Phys.* **8**, 213 (2006).
53. Ketterle, W. & Martin W. Z. Making, probing and understanding ultracold Fermi gases. *La Rivista del Nuovo Cimento* **31**, 247–422 (2008).
54. Grimm, R., Weidemüller, M. & Ovchinnikov, Y. in *Advances in Atomic, Molecular, and Optical Physics* (eds Bederson, B. & Walther, H.) Vol. 42, 95–170 (Elsevier, 2000).
55. Karpa, L. *Trapping Single Ions and Coulomb Crystals with Light Fields* (Springer, 2019).
56. Maxwell, J. *A Treatise on Electricity and Magnetism* Vol. 1 (Clarendon, 1873).
57. Krüchow, A. et al. Energy scaling of cold atom–atom–ion three-body recombination. *Phys. Rev. Lett.* **116**, 193201 (2016).

58. Pérez-Ros, J. & Greene, C. H. Universal temperature dependence of the ion–neutral–neutral three-body recombination rate. *Phys. Rev. A* **98**, 062707 (2018).
59. Pérez-Ros, J. & Greene, C. Communication: Classical threshold law for ion–neutral–neutral three-body recombination. *J. Chem. Phys.* **143**, 041105 (2015).
60. Mohammadi, A. et al. Life and death of a cold BaRb⁺ molecule inside an ultracold cloud of Rb atoms. *Phys. Rev. Res.* **3**, 013196 (2021).
61. Breit, G. & Rabi, I. Measurement of nuclear spin. *Phys. Rev.* **38**, 2082–2083 (1931).
62. Zhang, J. et al. *P*-wave Feshbach resonances of ultracold ⁶Li. *Phys. Rev. A* **70**, 030702 (2004).
63. Mies, F., Williams, C., Julienne, P. & Krauss, M. Estimating bounds on collisional relaxation rates of spin-polarized ⁸⁷Rb atoms at ultracold temperatures. *J. Res. Natl Inst. Stand. Technol.* **101**, 521–535 (1996).
64. Tschersbul, T., Brumer, P. & Buchachenko, A. Spin–orbit interactions and quantum spin dynamics in cold ion–atom collisions. *Phys. Rev. Lett.* **117**, 143201 (2016).
65. Wille, E. et al. Exploring an ultracold Fermi–Fermi mixture: interspecies Feshbach resonances and scattering properties of ⁶Li and ⁴⁰K. *Phys. Rev. Lett.* **100**, 053201 (2008).
66. Tiecke, T., Goosen, M., Walraven, J. & Kokkelmans, S. Asymptotic-bound-state model for Feshbach resonances. *Phys. Rev. A* **82**, 042712 (2010).
67. Werner, H.-J., Knowles, P. J., Knizia, G., Manby, F. R. & Schütz, M. Molpro: a general-purpose quantum chemistry program package. *WIREs Comput. Mol. Sci.* **2**, 242–253 (2012).
68. Goerz, M. H., Reich, D. M., Tomza, M. & Koch, C. QDYN, version 1.0, a program package for quantum dynamics and control (2015); <https://qdyn-library.net>

Acknowledgements This project has received funding from the European Research Council (ERC) under the European Union's Horizon 2020 research and innovation programme (grant number 648330) and was supported by the Georg H. Endress foundation. P.W., F.T. and T.S. acknowledge support from the DFG within the GRK 2079/1 programme. P.W. gratefully acknowledges financial support from the Studienstiftung des deutschen Volkes. L.K. is grateful for financial support from Marie Curie Actions. D.W., A.W. and M.T. acknowledge the financial support from the National Science Centre Poland (grant numbers 2016/23/B/ST4/03231 and 2020/36/T/ST2/00591) and Foundation for Polish Science within the First Team programme co-financed by the European Union under the European Regional Development Fund. K.J. acknowledges support from the Polish National Agency for Academic Exchange (NAWA) via the Polish Returns 2019 programme. The computational part was partially supported by the PL-Grid Infrastructure. We thank O. Dulieu for discussions. We thank M. Debatin for building the experimental apparatus.

Author contributions T.S. conceived the experiments. P.W. and F.T. contributed equally to the construction of the setup, carrying out of the experiments, discussion of the results and analysis of the data and were supported by L.K. and T.W. D.W., A.W., K.J. and M.T. performed theoretical calculations and analysis supervised by M.T. T.S. supervised the work. P.W. and T.S. wrote the manuscript with contributions from T.W., K.J. and M.T. All authors worked on the interpretation of the data and contributed to the final manuscript.

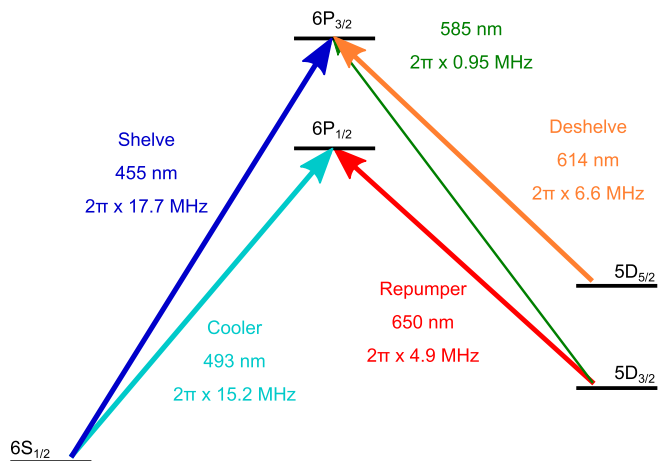
Competing interests The authors declare no competing interests.

Additional information

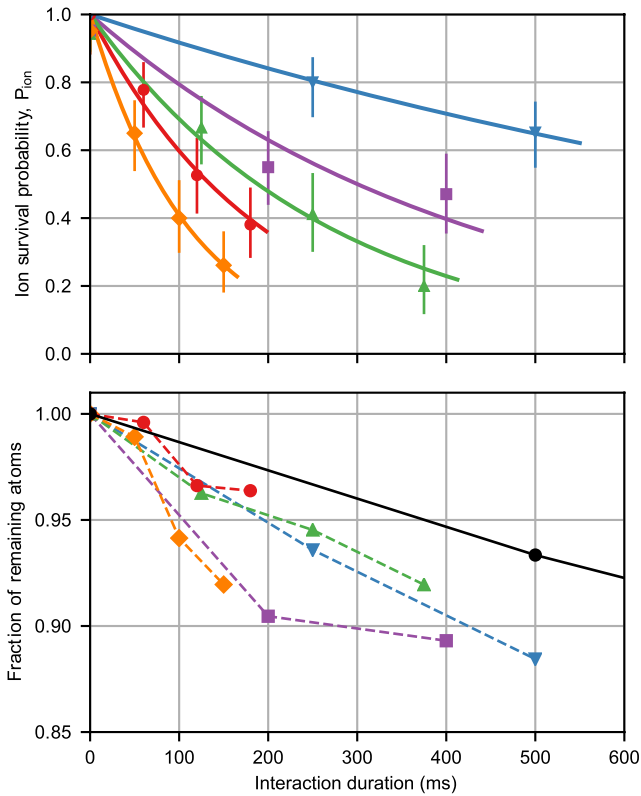
Correspondence and requests for materials should be addressed to Pascal Weckesser.

Peer review information *Nature* thanks Takashi Mukaiyama and the other, anonymous, reviewer(s) for their contribution to the peer review of this work.

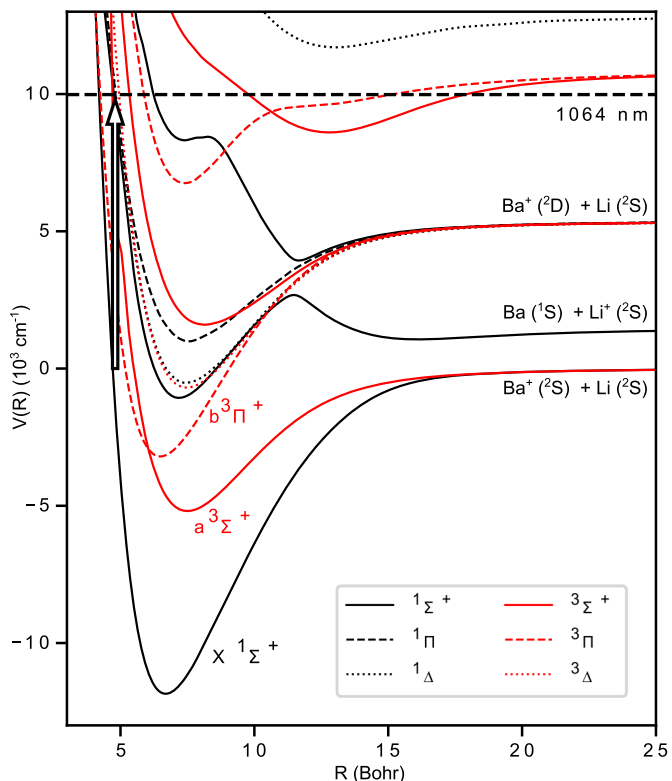
Reprints and permissions information is available at <http://www.nature.com/reprints>.



Extended Data Fig. 1 | Electronic level scheme of $^{138}\text{Ba}^+$ ($I=0$). We label the relevant electronic dipole transitions with their respective wavelength λ and natural linewidth Γ . We Doppler cool the ion driving the $6S_{1/2} \leftrightarrow 6P_{1/2}$ and $5D_{3/2} \leftrightarrow 6P_{1/2}$ transition. Inelastic losses, such as TBR followed by light-assisted dissociation, can partially result in the ion's population of the $5D_{5/2}$ manifold⁶⁰. We detect these events through optical pumping with 614 nm laser light, followed by fluorescence detection while Doppler cooling.



Extended Data Fig. 2 | Time-dependent Ba⁺ and Li loss for variable atomic density n around 296.31 G. (upper) Ion survival probability while interacting with the ⁶Li cloud for various atomic densities n . Data points are an average of at least 20 independent experimental realizations. Error bars denote the upper bound of the 1σ -confidence interval of the underlying binomial distribution. The solid lines are exponential fits ($e^{-t_{\text{int}}\Gamma_{\text{Loss}}}$) to the respective data. The fit results and the respective error bars are illustrated as density-dependent loss rate $\Gamma_{\text{Loss}}(n)$ in Fig. 3. (lower) Normalized number of remaining ⁶Li atoms interacting with a single ¹³⁸Ba⁺ ion in dependence on t_{int} . The markers and the respective colors indicate the association to the data in the upper graph. Li atoms are removed from the xODT by either spin-changing collisions or elastic atom-ion interactions. For the presented analysis, we exclude experiments resulting in ion loss, to avoid systematic errors by inelastic collisions. To mitigate the density uncertainty due to the decay of the atom number, we choose interaction durations resulting in maximal atom loss of $\leq 10\%$. We further indicate the atom number evolution in absence of interaction (black circles and solid line).



Extended Data Fig. 3 | Potential energy curves for a Ba⁺ ion interacting with a Li atom. The interaction between ground-state Ba⁺ ion and Li atom results in two molecular electronic states of the singlet $X^1\Sigma^+$ (solid black line) and triplet $a^3\Sigma^+$ (solid red line) symmetries. The excited molecular electronic state of the triplet $b^3\Pi$ symmetry (dashed red line) originates from the interaction of Ba⁺ ion in the lowest excited 2D state and ground-state Li atom and crosses the $a^3\Sigma^+$ state at a small interatomic distance. This crossing combined with SOC between $a^3\Sigma^+$ and $b^3\Pi$ states results in large second-order SOC in the collision channels responsible for the observed Feshbach resonances. Further illustrated is a possible photodissociation transition induced by our xODT laser operated at 1064 nm. The observed TBR might result in the formation of weakly-bound molecular ions. These can couple by laser light to higher energetic asymptotes, resulting in the population of excited states, including Ba⁺($5D_{5/2}$).

Article

Extended Data Table 1 | List of observed Feshbach resonances for the entrance channel

B_0^{expt} (G)	Δ_0^{expt} (G)	$B_{0,s}^{\text{theo}}$ (G)	t_{int} (ms)
80.47(21)	4.2(1.1)	81.2	300
93.59(9)	1.6(4)		100
143.29(31)	5.3(1.3)	143.3	300
157.42(19)	2.2(7)		300
165.4(4)	4.0(1.1)		300
173.0(2)	2.5(5)	172.5	300
270.86(5)	0.76(24)		300
272.59(3)	0.4(1)		300
296.31(19)	3.4(7)		300
307.38(14)	1.6(5)		200
316.31(11)	1.3(5)	316.4	200

$^{138}\text{Ba}^+|s\text{Ba}^+ = 1/2, m_s^{\text{Ba}^+} = -1/2) + ^6\text{Li}|f^{\text{Li}} = 1/2, m_f^{\text{Li}} = -1/2)$. The presented errors equal the 1 σ confidence interval of the fit. We can further assign an overall systematic error of 60 mG on δB_0^{expt} , including daily drifts and calibration uncertainties. We compare our measurements with an ABM and can assign four s-wave resonances $B_{0,s}^{\text{theo}}$ for $a_S = 0.236 R_4$ and $a_T = -0.053 R_4$.